Surface & Coatings Technology 326 (2017) 156–164

Contents lists available at ScienceDirect

Surface & Coatings Technology

journal homepage: www.elsevier.com/locate/surfcoat

Corrosion behavior of reactive sputtered Ti/TiN nanostructured coating and effects of intermediate titanium layer on self-healing properties

Sajjad Ghasemi [a], Ali Shanaghi [a,*], Paul K. Chu [b]

[a] Materials Engineering Department, Faculty of Engineering, Malayer University, Malayer, Iran
[b] Department of Physics and Department of Materials Science and Engineering, City University of Hong Kong, Tat Chee Avenue, Kowloon, Hong Kong, China

ARTICLE INFO

Article history:
Received 6 June 2017
Revised 11 July 2017
Accepted in revised form 20 July 2017
Available online 21 July 2017

Keywords:
Ti/TiN nanostructured coatings
Reactive sputtering
Corrosion resistance
Al 7075
Self-healing property

ABSTRACT

The 7xxx series aluminum alloys are anodic compared to the 1xxx series and other aluminum alloys due to the zinc content. In this work, Ti/TiN coatings are deposited on the7075 aluminum substrate by reactive magnetron sputtering and the corrosion resistance and self-healing properties are investigated. The coatings consist of TiN, TiO_xN_y, and TiO_2 phases. Electrochemical polarization and impedance studies reveal desirable features of the nanostructured Ti/TiN coating. The charge transport resistance increases by a factor of 20 compared to the Al 7075 substrate. Impedance tests are performed after polarization to examine the self-healing behavior. An improvement of 1.9 times in the charge transport resistance and inductive loop is observed after immersion for 12 h compared to one hour after polarization.

1. Introduction

The 7xxx series aluminum alloys contain zinc, magnesium, and copper for strength enhancement. Copper-containing alloys which offer many desirable features such as medium to high strength, excellent toughness, and high workability have been used as structural materials in aircrafts for more than 50 years [1]. The use of copper-free alloys by the automobile, construction, and other industry has increased in recent years. The 7xxx series alloys are anodic compared to the 1xxx series and other aluminum alloys due to the zinc content, and copper-free 7xxx alloys offer attractive corrosion resistance similar to that of the 3xxx, 5xxx, and 6xxx alloys [2–3]. However, copper-containing 7xxx alloys such as 7049, 7050, 7075, and 7118 are less resistant to corrosion than copper-free alloys [3].

TiN films deposited by magnetron sputtering typically have a columnar microstructure and upon exposure to a corrosive environment, the defects and holes in the coatings provide paths for penetration of corrosive media [4–6]. Nanostructured TiN coatings typically do not have adequate adhesion to metal substrates and also accelerate galvanic pitting [4–6]. Therefore, addition of a middle Ti layer or formation of multiple Ti/TiN layers is usually implemented [5–6]. The corrosion resistance of nanostructured Ti/TiN multilayered coatings can be controlled [7] and common deposition techniques include magnetron sputtering [8], laser ablation [9], pulsed laser deposition (PLD) [10], ion plating [11], vacuum arc [12], and arc ion plating [13]. In common multi-layer coatings Ti/TiN deposited on martensitic stainless steel and silicon [14–15], the columnar TiN layer thickness is between 100 and 200 nm and the thickness of the Ti intermediate layer varies from 10 to 30 nm [16]. In this work, nanostructured TiN hard coatings are deposited on 7075 aluminum which is considered a soft substrate by reactive magnetron sputtering together with Ti intermediate layers to improve the ductility, toughness, and adhesion of the hard coating. The structure, composition, morphology, corrosion resistance, and self-healing properties are investigated systematically.

2. Experimental details

Round 7075 aluminum samples with a radius of 1 cm were ground with 800, 1000, 1200, 2500, 3000, and 4000 SiC papers and 0.1 to 0.3 μm alumina pastes. The polished samples were degreased ultrasonically in acetone, alcohol, and distilled water. Before the Ti/TiN films were deposited by reactive magnetron sputtering driven by RF, argon ion sputtering was performed to clean the sample surface. The distance between the target and substrate was 10 cm and a titanium middle layer was deposited before nitrogen was bled into the vacuum chamber to deposit the TiN films on Al 7075. The important parameters used to deposit the structure comprising 6 alternating layers of Ti and TiN on Al 7075 illustrated in Fig. 1 are listed in Table 1.

The phase, structure, chemical composition, and morphology of the nanostructured coatings were examined by glancing-incidence X-ray diffraction (GIXRD, Philips PW-1730 X-ray diffractometer,

* Corresponding author.
E-mail address: a.shanaghi@malayeru.ac.ir (A. Shanaghi).

http://dx.doi.org/10.1016/j.surfcoat.2017.07.046
0257-8972/

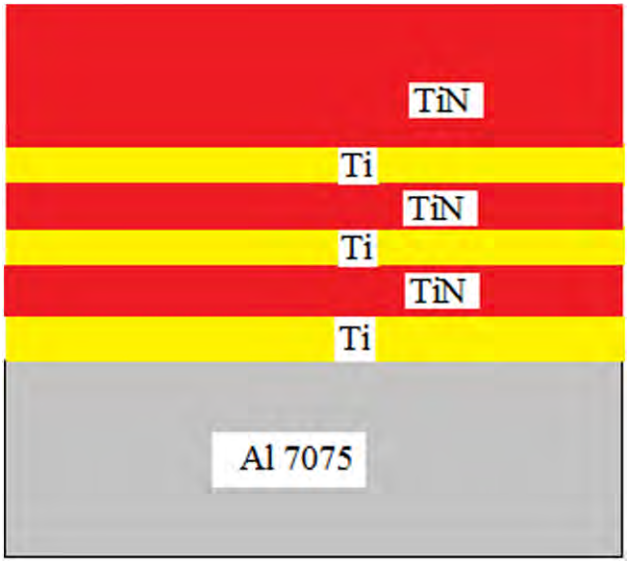

Fig. 1. Structure of the Ti/TiN multilayerd coating on Al 7075.

$CuK_{\alpha}\lambda = 0.154056\ nm$), X-ray photoelectron spectroscopy (XPS), field-emission scanning electron microscopy (FE-SEM, JSM7001F), and atomic force microscopy (AFM, Nanoscope V MultiMode System, Veeco), respectively. The thickness of the coating was determined by two methods, cross section examination and XPS depth profiling. The corrosion behavior was evaluated by performing electrochemical impedance and potentiodynamic polarization tests in a cell composed of the working, reference, and auxiliary electrodes in 250 ml of 3.5% NaCl aqueous solution on the Zennium Electrochemical Workstation potentiostat-galvanostat and ZView analysis software. To investigate the mechanism of self-healing of the Ti/TiN multilayers, impedance tests were performed at 1 and 12 h, followed by potentiodynamic polarization analyses as a destructive test after immersion in 3.5% NaCl for 72 h.

3. Results and discussion

3.1. Phase and structure properties

The GIXRD results in Fig. 2 are acquired at 3°, 5°, and standard 2 theta incident angle to determine the phases of the Ti/TiN coatings and the peaks are indexed to ICCC-JCPDS titanium nitride No. 38-1420, 7075 aluminum No.01-1176, and titanium No. 01-1197 showing that Ti and TiN have the hcp and fcc crystal structures, respectively. The Ti layer shows the most intense (002) peak at 38.60° and the most intense (111) peak of TiN is observed at 36.92° instead of other peaks in the GIXRD curves, suggesting the Ti (002) and TiN (111) preferred directions and that most of the TiN (111) planes are on the Ti (002) planes [17]. The sharp peak in the normal angle curve observed at 78.63° is related to Al (113) which overlaps TiN (222) in other incidence angles. Ti and TiN show several peaks at different diffraction angles and the intensity changes with angles. The monoclinic TiN shows peaks at 3° and 5° and in GIXRD at approximately 45°, 65°, and 78° 2-theta angles [18]. TiN shows two crystallographic structure, fcc and monoclinic, and fcc is predominant.

The size of the TiN nanostructure crystallite is estimated by Scherrer equation [19,20]:

$$L_{hkl} = \frac{k.\lambda}{\beta_{hkl}.\ \cos\theta_{hkl}} \quad (1)$$

where $(FWHM)_{hkl}\beta_{hkl}$ is in radians, θ_{hkl} is the Bragg angle,k is the Scherrer constant (which equals 0.9 for spherical grains), and λ is the wave length of the X-ray (0.1541874 *nm*). The crystallite sizes of Ti (002) and TiN (111) are 28.5 and 34 nm, respectively, similar to those reported by Sabramanian et al. [17].

XPS shows the presence of Ti, N, O, and C in the Ti/TiN coatings (Fig. 3a). According to the NIST XPS database [21], the $Ti2p_{1/2}$ peak at 464.8 eV is associated with TiN and TiO_2 and that at 459.2 eV corresponds to TiON and TiO_2 [22]. The N1 s spectrum at 397.6 eV can be assigned to N—C in the form of TiO_xN_y [17]. The O1s peak at 531.2 eV is related to TiO_2, Ti—O, and Ti—O bulk [14]. The C1s peak at 287.2 eV is ascribed to C or CO, C—, and C═O [17] arising from contamination [23]. The XPS depth profile is presented in Fig. 3b. Because of ion beam mixing during sputtering, the depth profiles deviate from the ideal ones resulting in non-rectangular features. The thickness of the Ti, TiN bottom layer, and TiN top layer is about 150, 200 and 550 nm, respectively, based on the estimated sputtering rate of 12.5 nm/min.

Fig. 4a and b show the surface morphology of the TiN coating and Fig. 4c indicates uniform and homogeneous Ti/TiN nanostructured coatings. As shown in Fig. 4b, the size of islands is between 20 and 100 nm and each island is made of tiny particles. Fig. 4c confirms the thickness of Ti and TiN coatings determined by XPS depth profiling (Fig. 3b) and shows that the grain boundaries of TiN coatings grow perpendicular to the substrate. The microstructure compatible with the T region is consistent with the Thornton model [24] and the columnar growth is disrupted by the Ti intermediate layer [25]. The columnar structure of titanium nitride can be disrupted in two ways by decreasing nitrogen at the interface between Ti and TiN and island and granular growth of Ti as an intermediate layer. To avoid creating tension between the layers, continuous coatings are selected. Fig. 4d shows the Ti, N, and O maps generally indicating a uniform and homogeneous composition. The uniform distribution of O may be represents thermodynamic stability and sustainability of the kinematics under the coating conditions. However, this theory requires further research. Fig. 4f shows that the nanostructured Ti/TiN coatings have a columnar structure and R_{rms} of 142 *A* which is almost half of the value previously reported [26].

3.2. Electrochemical properties

Although transition metal nitrides have high corrosion resistance, PVD coatings tend to have cracks, holes, and cavities through which the corrosion medium can access the substrate [27]. There are more interfaces in multi-layer coatings and some of the micro-cavities are blocked thus improving the corrosion resistance compared to single-layer coatings [28]. The Nyquist and Bode diagrams acquired after immersion in 3.5% NaCl for 1, 48, 60, and 72 h are depicted in Figs. 5, 6, and 7 respectively. When the sample is in an electrolyte, the defects in the nanostructured coating allow rapid penetration of the corrosive medium and local galvanic corrosion cells are formed [29]. The local corrosion rate is important and as shown in Fig. 5, the charge transport resistance at low frequencies suggests improved corrosion resistance in the presence of the coating. Figs. 6 and 7 show two time constants due to mismatch of the surface structure [30] and two different interfacial reactions. Generally, the time constant at high frequencies can be attributed to the resistive behavior of defects (cavities and cracks) in the nanostructured coating and that at low frequencies are related to the

Table 1
Ti/TiN multilayer nanostructured coating deposition parameters.

Parameter	Time (min)	Power (watt)	pressure (mtorr)	Ar gas flow (sccm)	N_2 gas flow (sccm)
Ti layer	15	220–280	3.2	14–17	–
TiN sublayer	25	220–280	4.4	14–17	8–10
TiN final layer	60	220–280	4.4	14–17	8–10

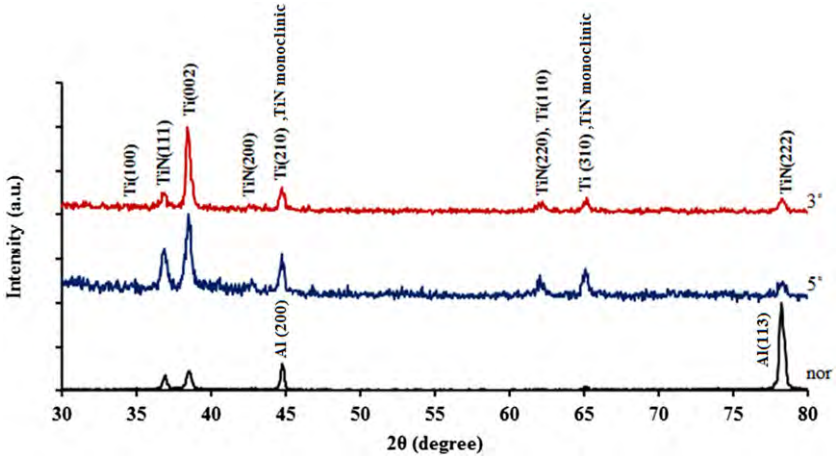

Fig. 2. GIXRD patterns acquired at 3° and 5°, and standard 2 theta angle from the multilayered Ti/TiN nanostructured coating.

interfacial layer [31,32]. The impedance modulus of the nanostructured coating shows high impedance at low frequencies and it is more than that of the native oxide layer on aluminum. As shown in Fig. 6, the impedance of the nanostructured coating is reduced after immersion for 48 h probably due to penetration of the solution, and the impedance modulus of the coating is constant and stable until the end of

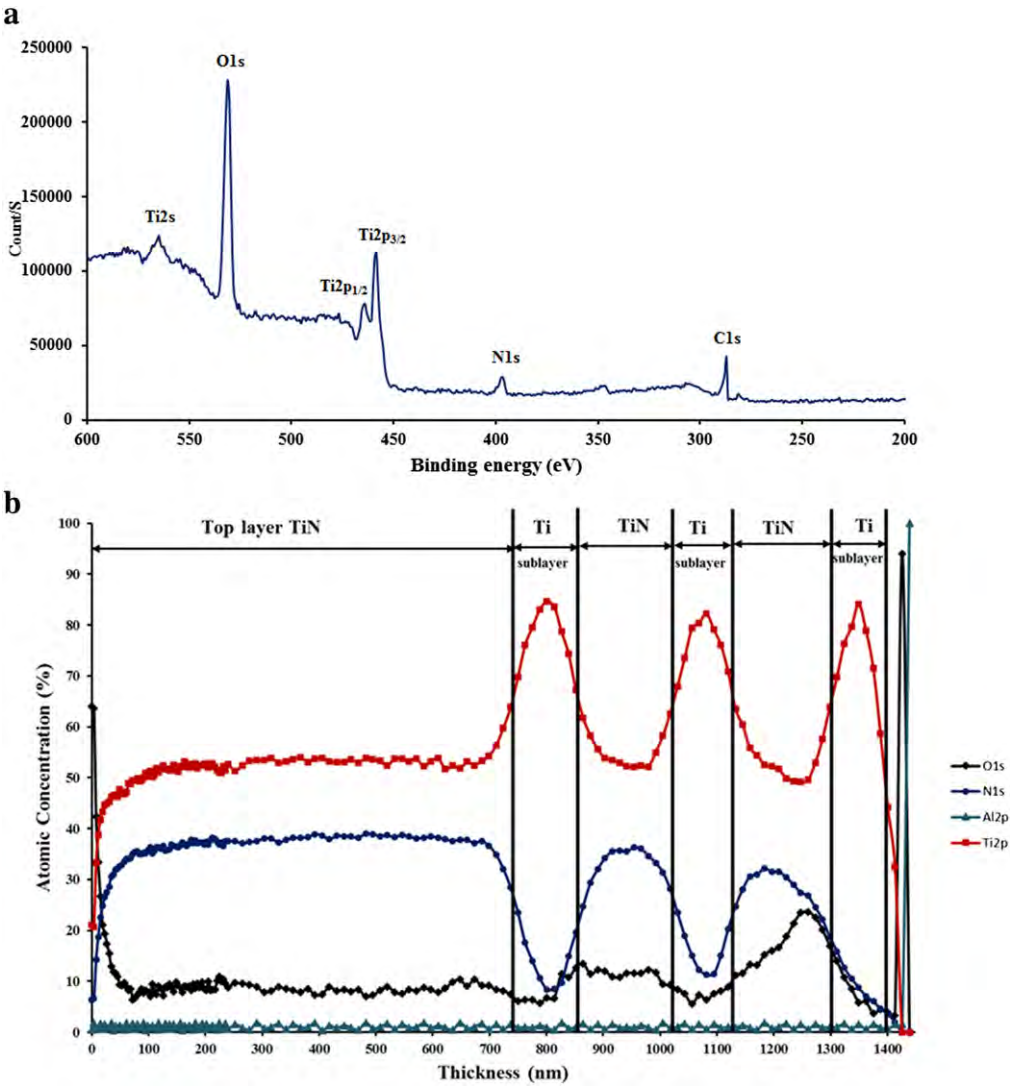

Fig. 3. (a) XPS spectra acquired from the surface of the Ti/TiN nanostructured coating, and (b) XPS depth profiles of the Ti/TiN nanostructured coating.

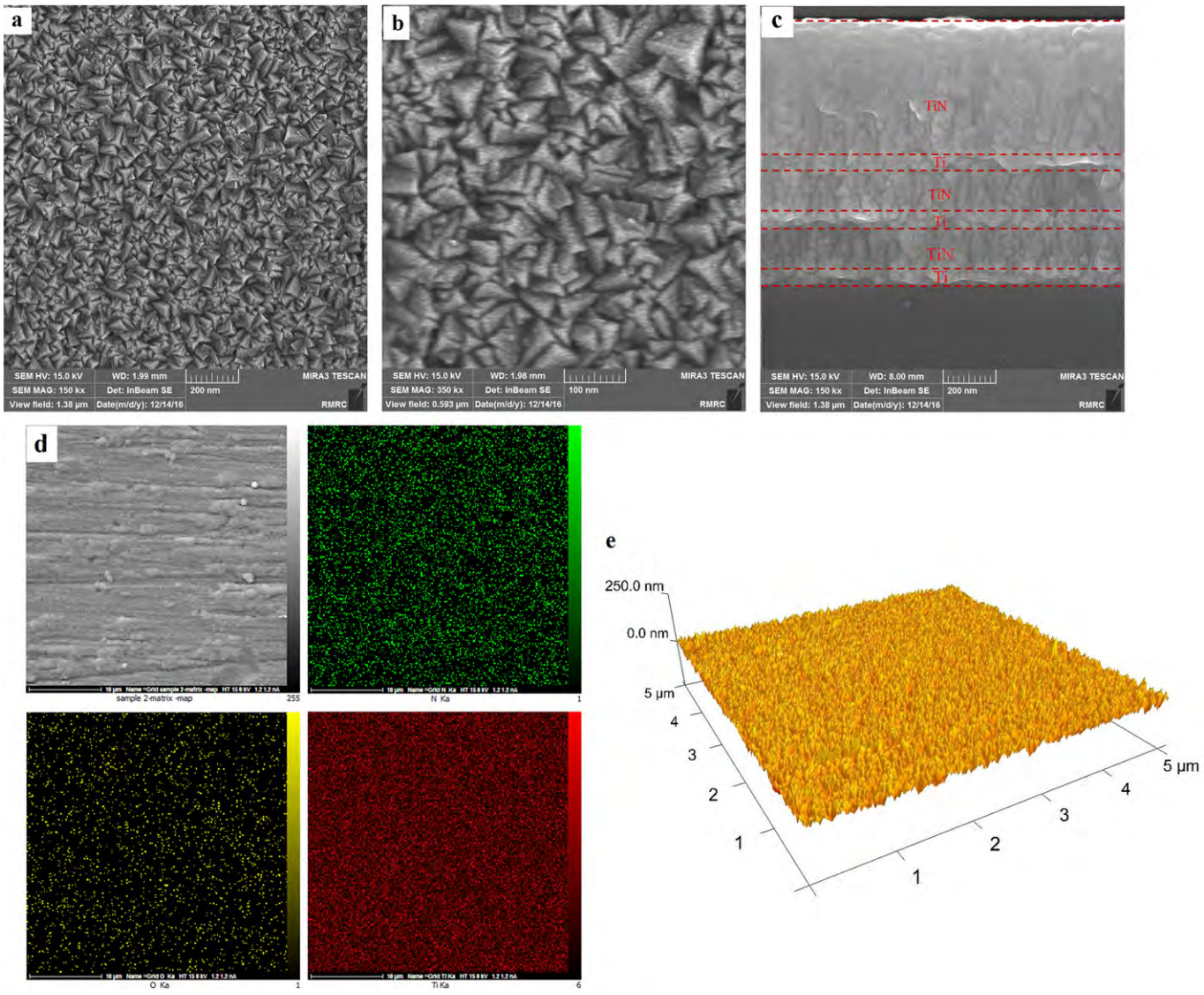

Fig. 4. FE-SEM images of the surface of the TiN coating at different magnifications (*a*) 150Kx, and (*b*) 350Kx, (*c*) FE-SEM images of the cross-section of the multi-layered coating, (*d*) Elemental maps of the coating cross-section; (*e*) AFM image of the Ti/TiN nanostructured coating.

immersion. The TiN layer possibly forms a TiO_2 film in the presence of oxygen according to Eq. (2) [33]:

$$TiN + O_2 \rightarrow TiO_2 + {}^{1}/_{2}N_2 \qquad \Delta G = -\frac{139kcal}{mol} \tag{2}$$

Reduction of the impedance modulus with immersion time from 48 to 60 h is very small, confirming the excellent resistance of the coating. The impedance is constant after 60 h and increases after 72 h due to formation of TiO_2 and reactions of the Ti middle layer. Fig. 7 shows that the high frequency peaks are related to the coating. No steady reduction or increasing trend is observed from the peaks and the peak intensity decreases because of charge transport and water absorption [31,34], consequently changing the capacitive behavior to a resistive one. The larger peak intensity is attributed to the formation of TiO_2 which increases the phase difference between the voltage and current thus rendering the system to behave in a capacitive manner. According to Fig. 7, as the immersion time is increased from 1 h to 48 h, the capacitive behavior increases because of blocking defects in TiN and the Ti intermediate layer improves the resistance of the coating by acting as a barrier against corrosive ions. In addition, by increasing the immersion time to 60 h, the corrosion resistance decreases drastically because of destruction of the titanium nitride layer by penetration of corrosive ionsor uptake the water. When the immersion time is increased to 72 h, an

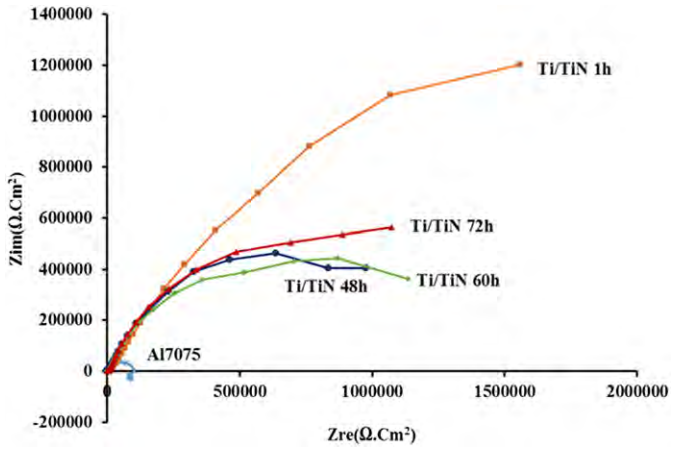

Fig. 5. Nyquist plot acquired at different time points during immersion in 3.5 wt% NaCl solution.

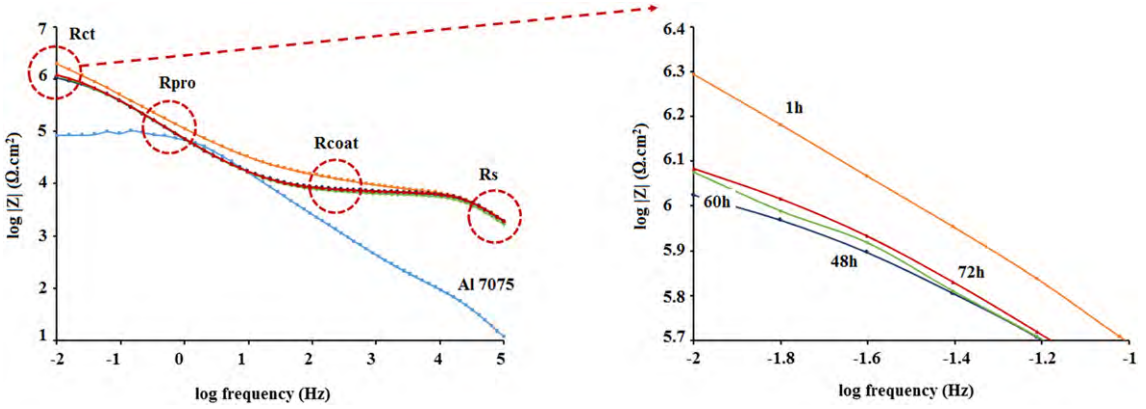

Fig. 6. Bode diagrams obtained at different time points during immersion in 3.5 wt% NaCl solution.

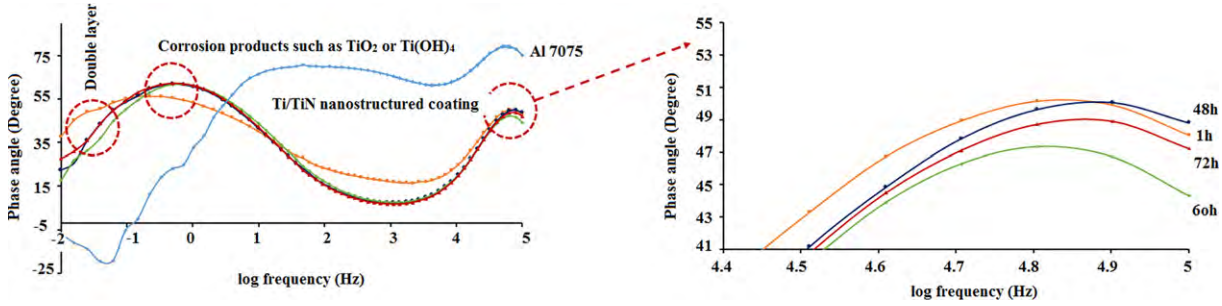

Fig. 7. Bode-phase diagrams obtained at different time points during immersion in 3.5 wt% NaCl solution.

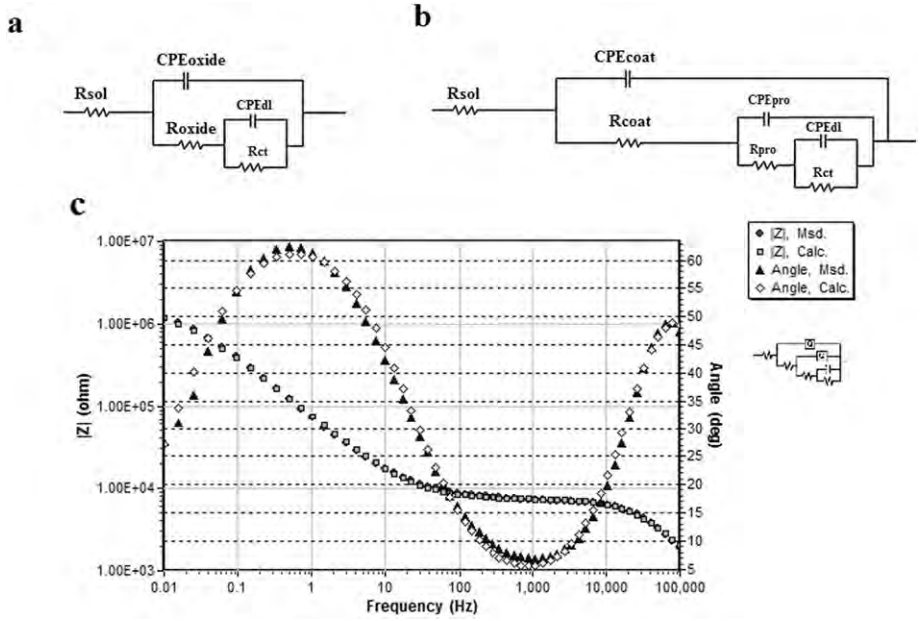

Fig. 8. Equivalent circuits of: (a) Al 7075; (b) Nanostructured coating before and after polarization test; (c) Fitted curve of the Ti/TiN coating after immersion for 72 h.

Table 2
Parameters obtained from the equivalent circuits.

Samples	Time (h)	R_{sol} ($\Omega.Cm^2$)	R_{coat} ($\Omega.Cm^2$)	CPE_{coat} ($\mu F.cm^{-2}.s^{n-1}$)	n_{coat}	R_{Pro} ($\Omega.Cm^2$)	CPE_{Pro} ($\mu F.cm^{-2}.s^{n-1}$)	n_{pro}	R_{oxide} ($\Omega.Cm^2$)	CPE_{oxide} ($\mu F.cm^{-2}.s^{n-1}$)	n_{oxide}	R_{ct} ($\Omega.Cm^2$)	CPE_{dl} ($\mu F.cm^{-2}.s^{n-1}$)	n_{dl}
Al 7075	1	84	–	–	–	–	–	–	112,475	1.63	0.81	96,473	0.17	–
Ti/TiN coating	1	143	6081	1.03E-3	–	12,785	7.78E-1	0.71	–	–	–	6,994,735	1.85	0.68
	48	106	5972	8.11E-4	–	6731	9.41E-3	0.67	–	–	–	1,437,291	3.38E-3	0.76
	60	91	5865	3.84E-3	0.91	6298	3.32	0.75	–	–	–	1,405,286	8.89E-5	–
	72	93	6579	2.86E-3	0.93	181,743	3.39	0.76	–	–	–	1,495,361	3.12E-4	–
Ti/TiN coating after polarization	1	87	7236	1.94E-3	0.93	307,146	4.81	0.69	–	–	–	200,163	14.97	–
	12	115	6653	1.02E-3	–	21,118	1.41	0.92	–	–	–	381,345	1.52	0.97

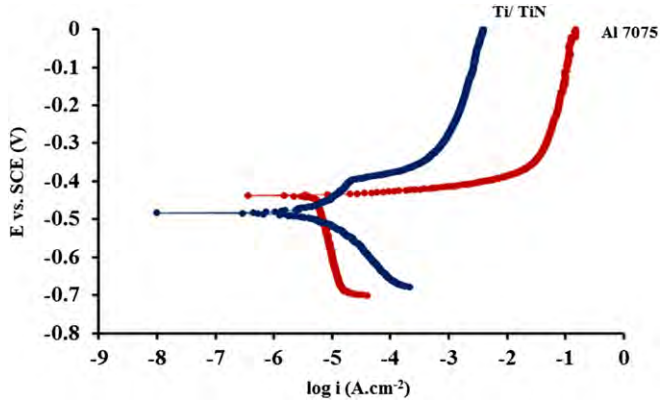

Fig. 9. Potentiodynamic polarization diagrams of the Al 7075 and Ti/TiN nanostructured coating.

Table 3
Electrochemical parameters obtained from 3.5 wt% NaCl solution by Tafel extrapolation.

Sample	E_{corr}(V)	i_{corr}(A/cm^2)*10^{-6}	R_p(ohm)	C.R(mm/y)	P(%)
Ti/TiN	−0.4808	0.5367	5344	0.006729	66
Al 7075	−4346	1.577	896.5	0.0172	–

intermediate layer of titanium causes restoration and blocking defects thereby producing improved resistance and capacitive behavior.

The equivalent circuit in Fig. 8a is for Al 7075. R_s related to the solution resistance, R_{oxide} and CPE_{oxide} are related to the oxide layer, and R_{ct} and C_{dl} to the charge transfer resistance, and capacitive double layer, respectively. Fig. 8b represents the nanostructured coating, in which R_{coat} and CPE_{coat} in the equivalent circuit are associated with the Ti/TiN coating and interfacial reaction between the coating and electrolyte and R_{pro} and CPE_{pro} are related to the reactions at the interface between the middle *Ti* layer and electrolyte. Two elements are added to the equivalent circuit to calculate the capacity of the dual layer (CPE_{dl}) and polarization resistance (R_{ct}). To demonstrate the viability of the equivalent circuit, the fitted curve of the Ti/TiN nanostructured coating after immersion for 72 h in 3.5% NaCl is shown in Fig. 8c. The calculated parameters (Table 2) suggest that the coating provides enhanced corrosion resistance compared to the uncoated aluminum. Between 48and 72 h (end of immersion), a rather steady trend is observed from the charge transport due to the formation of a stable oxide layer at the interface between the electrolyte and substrate/intermediate layer [35]. The results suggest that the solution does not penetrate to the substrate to cause damage.

The potentiodynamic polarization curves of the nanostructured coating and Al 7075 substrate are presented in Fig. 9. The corrosion current density (i_{corr}) and corrosion potential (E_{corr}) are obtained by extrapolation of the linear region in the Tafel diagram in Fig. 9. The protective effect (%) of the nanostructured coating is calculated by Eq. (3) [36]:

$$P = \left(1 - \frac{i_{corr}}{i^0_{corr}}\right) \times 100\% \quad , \tag{3}$$

where i_{corr} and i^0_{corr} are the corrosion current densities of the nanostructured coating and substrate, respectively. As shown in Table 3, the corrosion current density observed from the coating is less than that of the substrate. The corrosion potential is larger and corrosion current density is smaller than those reported previously [17]. It can be deduced

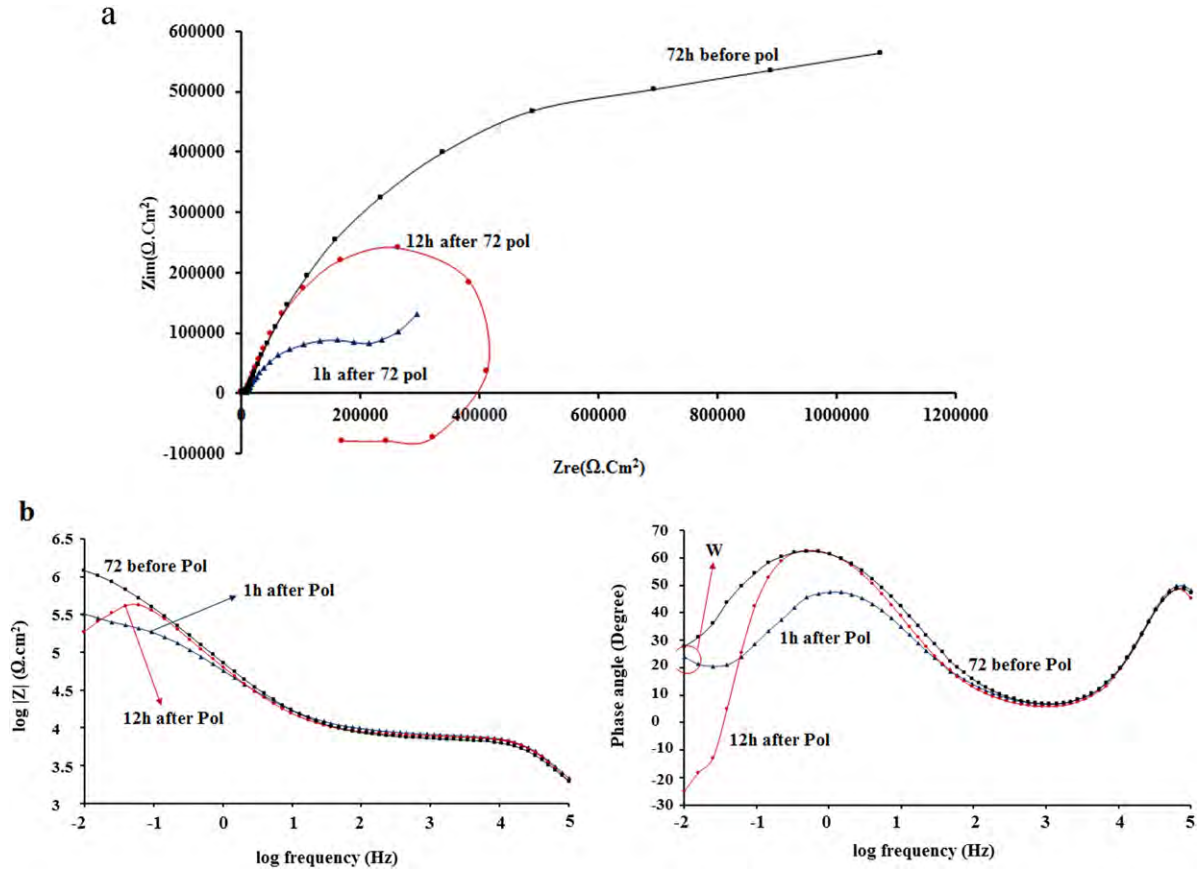

Fig. 10. EIS plots of the Ti/TiN nanostructured coating: (a) Nyquist diagram and (b) Bode diagram obtained at different immersion time points in 3.5 wt% NaCl solution after polarization test of 72 h.

from Table 3 that the protection efficiency of the substrate is 66% in the presence of the nanostructured coating and similar values have been reported [26]. Generally, holes are easily formed during formation of the columnar structure. The column boundaries and holes that are perpendicular to the nanostructured coating/substrate interface provide paths for the corrosive solution. In the multi-layered coating, the layered structure disrupts the growth of the columns thus impeding penetration of the corrosive solution [14,37]. Fig. 9 shows the formation of a passive TiO_2 layer [33,38] in the anodic branch at −0.398 V in the polarization diagram of the nanostructured coating. The corrosion rate is calculated from the two immersed samples by Faraday law (Eq. (4)) [39]:

$$\text{Corrosion rate}\left(\frac{mm}{y}\right) = 316 \times i_{corr} \times {}^{M}/_{z} \times F \times \rho., \quad (4)$$

where i_{corr} is the corrosion current density (A/cm^2) obtained from the potentiodynamic polarization curves, M is the molar weight of the metal (g/mol), z is the number of transported electrons for each metallic ion, F the Faraday constant, and ρ the density of the metal (g/cm^2). The nanostructured coating shows a smaller corrosion rate than the substrate and the former shows 6-fold increase in the corrosion resistance. Indeed, formation of TiO_2 and insoluble compounds such as $Ti(OH)_4$ in the cathodic area, which is damaged by water absorption or penetration of chloride ions leading to oxygen reduction, inhibits the oxygen supply to these areas and shifts the open circuit potential to a more negative value.

3.3. Self-healing behavior

After the polarization tests, the healing behavior or formation TiO_2 in the defects is investigated. After immersion for 1 h 3.5% NaCl, the Nyquist curve (Fig. 10a) shows a long tail at low frequencies suggesting a controlled corrosion behavior by forming the insoluble compound, faraday impedance [40] and active corrosion. The main process in Al corrosion in chloride related leading to the formation and growth of cavities. These cavities are often created around intermetallic particles

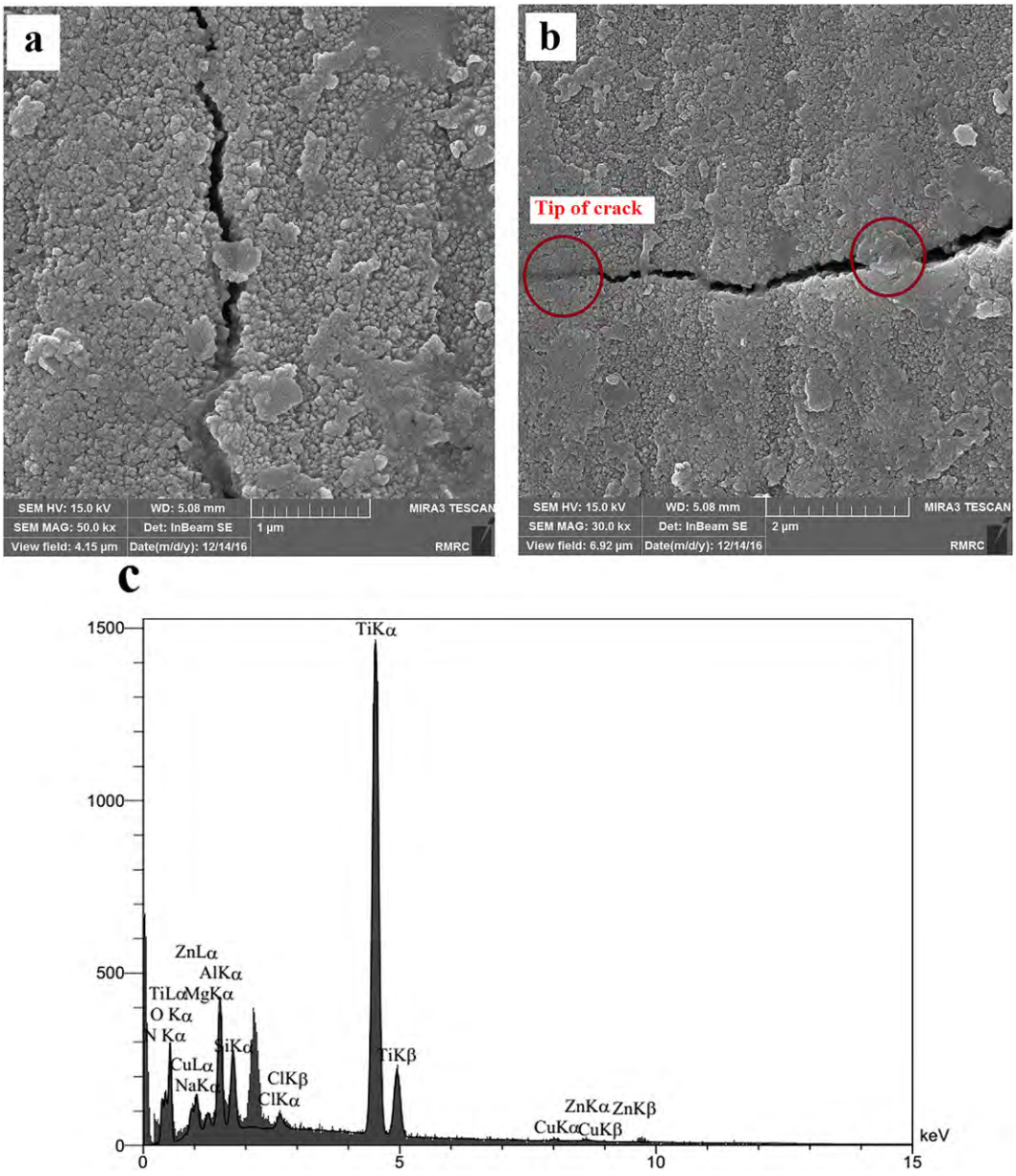

Fig. 11. FE-SEM images of the crack in the Ti/TiN nanostructured coating after polarization testing at two different magnifications: (a)50Kx, (b) 30Kx; and (c) EDS spectrum of the tip of the crack.

that are nobler than Al [41] and Jelkovic et al. [34] reported the formation of honeycomb metallic masses in these cavities.

The metals are rich in copper which has sufficiently nobler potentials and promotes cavity initiation and growth as effective cathodes. This copper honeycomb structure provides a diffusion-controlled path for the corrosion products and corrosive agents. The FE-SEM images show the cracks in the Ti/TiN nanostructured coating after polarization tests (Fig. 11a and b). However, the cavities are not visible from the substrate due to adequate resistance rendered by the nanostructured coating.

The circuit in Fig. 8b is proposed for the Ti/TiN nanostructured coating after the polarization test [42]. According to Table 2, larger R_{coat} and R_{pro} indicate the formation of TiO_2 or insoluble compound at the interface of Ti/TiN coating in 3.5 wt% NaCl solution. The diameter of the Nyquist semi-circle is related to the coating at low frequencies increases after 12 h and the low-frequency phase angle in Fig. 10b increases verifying the formation of a stable TiO_2 layer and healing ability. Healing occurs as cracks are closed as shown in Fig.11a and b and the possible reactions to form TiO_2 or $Ti(OH)_4$ are shown in the following [29]:

$$Ti - 4e^- Ti^{4+} \quad (5)$$

$$O_2 + 2H_2O + 4e^- \rightarrow 4OH^- \quad . \quad (6)$$

The presence of Ti and O in the EDS spectrum of the tip of crack may block the cracks (Fig. 11c). An inductive behavior is observed at low frequencies due to surface adsorption, corrosion products, and formation of the TiO_2 or $Ti(OH)_4$ on the corroded Ti/TiN coating. Both adsorption and electrochemical procedures are potential-dependent and the outcome of this dependence is the displacement of the induction phase in the cell current. According to the Bode diagram (Fig. 10b), after polarization for 1 h, the capacitive behavior is shown representing healing at defects caused by polarization being destructive and the intermediate layer of titanium. By increasing the immersion time to 12 h, this behavior changes due to the formation of a protective layer at the interface between the Ti/TiN coating and substrate leading to increased resistance at low frequencies. The parameters obtained by fitting the equivalent circuit are presented in Table 2. TiO_2 is quite stable in the solution with low solubility in acidic and basic solutions (Pourbaix diagrams). EIS shows higher impedance at 12 h. The semi-conducting TiO_2 has a large band gap, low electrical conductivity [43], and high corrosion resistance and a higher corrosion resistance increases the impedance.

4. Conclusion

Nanostructured Ti/TiN coatings are deposited on 7075 aluminum which is considered a soft substrate by reactive magnetron sputtering driven by RF. The preferred direction of the sputtered Ti and TiN films with hcp and fcc structures are (002) and (111), respectively. The nanostructured coating has small grains and a rough surface. The corrosion resistance of the nanostructured coating is better than that of the Al 7075 substrate due to prevention of grain growth by introduction of the intermediate Ti layer, formation of TiO_2, and reactions of the Ti middle layer. Blocking of defects to TiN created by the Ti intermediate layer improves the corrosion resistance as a result of the barrier against corrosive ions. Formation of a stable TiO_2 or $Ti(OH)_4$layer produces the healing ability. Even after polarization for 12 h, enhancement of 91% is observed from the polarization resistance due to healing of cracks in the nanostructured coating.

Acknowledgements

The authors would like to thank the Iranian Nanotechnology Initiative Council. The work was financially supported by Malayer University Research Grant, Iran National Science Foundation and Hong Kong Research Grants Council (RGC) General Research Funds (GRF) No.·CityU 11301215, as well as City University of Hong Kong Applied Research Grants (ARG) Nos. 9667122 and 9667144.

References

[1] Y. Huanga, X. Yeb, B. Hu, L. Chen, Equivalent crack size model for pre-corrosion fatigue life prediction of aluminum alloy 7075-T6, Int. J. Fatigue 88 (2016) 217–226.
[2] W. Tian, S. Li, B. Wang, J. Liu, M. Yu, Pitting corrosion of naturally aged AA 7075 aluminum alloys with bimodal grain size, Corros. Sci. 113 (2016) 1–16.
[3] J.R. Davis, Corrosion of Aluminum and Aluminum Alloys, Asm International, 1999.
[4] Y.X. Ou, J. Lin, S. Tong, H.L. Che, W.D. Sproul, M.K. Lei, Wear and corrosion resistance of CrN/TiN superlattice coatings deposited by a combined deep oscillation magnetron sputtering and pulsed dc magnetron sputtering, Appl. Surf. Sci. 351 (2015) 332–343.
[5] D. Zhou, H. Peng, L. Zhu, H. Guo, S. Gong, Microstructure, hardness and corrosion behaviour of Ti/TiN multilayer coatings produced by plasma activated EB-PVD, Surf. Coat. Technol. 258 (2014) 102–107.
[6] E. Andrade, M. Flores, S. Muhl, N.P. Barradas, G. Murillo, E.P. Zavala, M.F. Rocha, Ion beam analysis of TiN/Ti multilayers deposited by magnetron sputtering, Nucl. Instrum. Methods Phys. Res., Sect. B 219–220 (2004) 763–767.
[7] M. Flores, S. Muhl, E. Andrade, The relation between the plasma characteristic and the corrosion properties of TiN/Ti multilayers deposited by unbalanced magnetron sputtering, Thin Solid Films 433 (1–2) (2003) 217–223.
[8] N. Saoula, S. Djerourou, K. Yahiaoui, K. Henda, R. Kesri, R. Erasmus, J. Comins, Study of the deposition of Ti/TiN multilayers by magnetron sputtering, Surf. Interface Anal. 42 (6–7) (2010) 1176–1179.
[9] G. Radhakrishnan, P.M. Adams, D.M. Speckman, Low temperature pulsed laser deposition of titanium carbide on bearing steels, Thin Solid Films 358 (1–2) (2000) 131–138.
[10] L. Major, J. Morgiel, B. Major, J.M. Lackner, W. Waldhauser, R. Ebner, L. Nistor, G. Van Tendeloo, Crystallographic aspects related to advanced tribological multilayers of Cr/CrN and Ti/TiN types produced by pulsed laser deposition (PLD), Surf. Nanostruct. Coatingings Technol. 200 (22 − 23) (2006) 6190–6195.
[11] R.F. Huang, L.S. Wen, L.P. Guo, J. Gong, B.H. Yu, H. Bangert, Microstructural and indentation characterization of Ti/TiN multilayer films, Surf. Nanostruct. Coatingings Technol. 50 (2) (1992) 97–101.
[12] W.-F. Wu, K.-L. Ou, C.-P. Chou, J.-L. Hsu, PECVD Ti/TiN x barrier with multilayered amorphous structure and high thermal stability for copper metallization, Electrochem. Solid-State Lett. 6 (2) (2003) G27–G29.
[13] M. Bromark, M. Larsson, P. Hedenqvist, S. Hogmark, Wear of PVD Ti/TiN multilayer nanostructured coatingings, Surf. Nanostruct. Coatingings Technol. 90 (3) (1997) 217–223.
[14] H.C. Barshilia, M. Surya Prakash, A. Poojari, K.S. Rajam, Corrosion behavior of nanolayered TiN/NbN multilayer nanostructured coatingings prepared by reactive direct current magnetron sputtering process, Thin Solid Films 460 (1–2) (2004) 133–142.
[15] J. Vossen and J. O'Neill Jr, RF sputtering processes, RCA Labs., Princeton, NJ1968.
[16] J.-H. Huang, Y.-P. Tsai, G.-P. Yu, Effect of processing parameters on the microstructure and mechanical properties of TiN film on stainless steel by HCD ion plating, Thin Solid Films 355 (1999) 440–445.
[17] B. Subramanian, R. Ananthakumar, M. Jayachandran, Structural and tribological properties of DC reactive magnetron sputtered titanium/titanium nitride (Ti/TiN) multilayered nanostructured coatingings, Surf. Nanostruct. Coatingings Technol. 205 (11) (2011) 3485–3492.
[18] P.D. Lomenzo, P. Zhao, Q. Takmeel, S. Moghaddam, T. Nishida, M. Nelson, C.M. Fancher, E.D. Grimley, X. Sang, J.M. LeBeau, J.L. Jones, Ferroelectric phenomena in Si-doped HfO_2 thin films with TiN and Ir electrodes, J. Vac. Sci. Technol., B: Microelectron. Nanometer Struct.–Process., Meas., Phenom. 32 (3) (2014) 1–8 (03D123).
[19] S. Logothetidis, P. Patsalas, C. Charitidis, Enhanced catalytic activity of nanostructured cerium oxide films, Mater. Sci. Eng. C 23 (6–8) (2003) 803–806.
[20] R. Yogamalar, R. Srinivasan, A. Vinu, K. Ariga, A.C. Bose, X-ray peak broadening analysis in ZnO nanoparticles, Solid State Commun. 149 (43–44) (2009) 1919–1923.
[21] C. Wagner, C.J. Powell, J. Allison, J. Rumble Jr., D. Blakeslee, M. Dal-Favero, NIST X-ray Photoelectron Spectroscopy Database (Version 2.0), Retrieved from NIST Standard Reference Data Program website, http://www. nist. gov/srd 1997.
[22] B. Subramanian, R. Ananthakumar, V.S. Vidhya, M. Jayachandran, Influence of substrate temperature on the materials properties of reactive DC magnetron sputtered Ti/TiN multilayered thin films, Mater. Sci. Eng. B 176 (1) (2011) 1–7.
[23] J.N. Musher, R.G. Gordon, Atmospheric pressure chemical vapor deposition of titanium nitride from tetrakis (diethylamido) titanium and ammonia, J. Electrochem. Soc. 143 (2) (1996) 736–744.
[24] J.A. Thornton, High rate thick film growth, Annu. Rev. Mater. Sci. 7 (1) (1977) 239–260.
[25] D. Zhou, H. Peng, L. Zhu, H. Guo, S. Gong, Microstructure, hardness and corrosion behaviour of Ti/TiN multilayer nanostructured coatingings produced by plasma activated EB-PVD, Surf. Nanostruct. Coatingings Technol. 258 (2014) 102–107.
[26] J. Bolton, X. Hu, In vitro corrosion testing of PVD nanostructured coatingings applied to a surgical grade Co–Cr–Mo alloy, J. Mater. Sci. Mater. Med. 13 (6) (2002) 567–574.
[27] H.A. Jehn, Improvement of the corrosion resistance of PVD hard nanostructured coatinging–substrate systems, Surf. Nanostruct. Coatingings Technol. 125 (1–3) (2000) 212–217.
[28] C.S. Lin, C.S. Ke, H. Peng, Corrosion of CrN and CrN/TiN nanostructured coatinged heat-resistant steels in molten A356 aluminum alloy, Surf. Nanostruct. Coatingings Technol. 146–147 (2001) 168–174.

[29] Q. Wan, H. Ding, M.I. Yousaf, Y.M. Chen, H.D. Liu, L. Hu, B. Yang, Corrosion behaviors of TiN and Ti-Si-N (with 2.9 at.% and 5.0 at.% Si) nanostructured coatingings by electrochemical impedance spectroscopy, Thin Solid Films 616 (2016) 601–607.
[30] A. Shanaghi, P.K. Chu, A.R.S. Rouhaghdam, R. Xu, T. Hu, Structure and corrosion resistance of Ti/TiC nanostructured coatingings fabricated by plasma immersion ion implantation and deposition on nickel–titanium, Surf. Nanostruct. Coatingings Technol. 229 (2013) 151–155.
[31] G. Yoganandan, K.P. Premkumar, J. Balaraju, Evaluation of corrosion resistance and self-healing behavior of zirconium–cerium conversion nanostructured coatinging developed on AA2024 alloy, Surf. Nanostruct. Coatingings Technol. 270 (2015) 249–258.
[32] L.E.M. Palomino, I.V. Aoki, H.G. de Melo, Microstructural and electrochemical characterization of Ce conversion layers formed on Al alloy 2024-T3 covered with Cu-rich smut, Electrochim. Acta 51 (26) (2006) 5943–5953.
[33] W.-G. Kim, H.-C. Choe, Effects of TiN nanostructured coatinging on the corrosion of nanostructured Ti–30Ta–xZr alloys for dental implants, Appl. Surf. Sci. 258 (6) (2012) 1929–1934.
[34] M. Zheludkevich, R. Serra, M. Montemor, K. Yasakau, I.M. Salvado, M. Ferreira, Nanostructured sol–gel nanostructured coatingings doped with cerium nitrate as pretreatments for AA2024-T3: corrosion protection performance, Electrochim. Acta 51 (2) (2005) 208–217.
[35] R. Akid, M. Gobara, H. Wang, Corrosion protection performance of novel hybrid polyaniline/sol–gel nanostructured coatingings on an aluminium 2024 alloy in neutral, alkaline and acidic solutions, Electrochim. Acta 56 (5) (2011) 2483–2492.
[36] R. Ananthakumar, B. Subramanian, A. Kobayashi, M. Jayachandran, Electrochemical corrosion and materials properties of reactively sputtered TiN/TiAlN multilayer nanostructured coatingings, Ceram. Int. 38 (1) (2012) 477–485.
[37] L.A.S. Ries, D.S. Azambuja, I.J.R. Baumvol, Corrosion resistance of steel nanostructured coatinged with Ti/TiN multilayers, Surf. Nanostruct. Coatingings Technol. 89 (1) (1997) 114–120.
[38] W.-G. Kim, H.-C. Choe, Y.-M. Ko, Electrochemical behaviors of a TiN-nanostructured coatinged/nanotube-formed Ti-Zr alloy, J. Korean Phys. Soc. 54 (3) (2009) 1036–1041.
[39] I. De Ryck, E. Van Biezen, K. Leyssens, A. Adriaens, P. Storme, F. Adams, Study of tin corrosion: the influence of alloying elements, J. Cult. Herit. 5 (2) (2004) 189–195.
[40] R. Wang, S. Luo, M. Liu, Y. Xue, Electrochemical corrosion performance of Cr and Al alloy steels using a J55 carbon steel as base alloy, Corros. Sci. 85 (2014) 270–279.
[41] R. Buchheit, R. Grant, P. Hlava, B. McKenzie, G. Zender, Local dissolution phenomena associated with S phase (Al2CuMg) particles in aluminum alloy 2024-T3, J. Electrochem. Soc. 144 (8) (1997) 2621–2628.
[42] D.W. Buzza, R.C. Alkire, Growth of corrosion pits on pure aluminum in 1M NaCl, J. Electrochem. Soc. 142 (4) (1995) 1104–1111.
[43] K. Chaudhuri, P. Mathur, T. Saxena, V. Bothra, A. Malhotra, Impurity-band conduction in heavily doped n-type GaAs, Phys. Rev. B 21 (2) (1980) 767.